Proceedings of Aerospace Europe Conference 2020 (AEC2020), 24-28
February 2020, Bordeaux, France. Paper number 00337

00337

MULTI-FIDELITY ASSESSMENT OF EXHAUST SYSTEMS FOR COMPLETE ENGINE-AIRFRAME CONFIGURATIONS

J. Hueso-Rebassa [(1)], F. Tejero [(2)], J. Otter [(3)], I. Goulos [(4)], D. MacManus [(5)]

[(1)] Cranfield University, MK43 0AL, Cranfield, UK, Email: J.Hueso-Rebassa@cranfield.ac.uk
[(2)(3)(4)(5)] Cranfield University, MK43 0AL, Cranfield, UK

KEYWORDS: Complete aircraft assessment, installed performance, non-axisymmetric exhaust systems, multi-fidelity analysis, co-kriging

ABSTRACT:

For podded underwing configurations, the goal of specific fuel consumption reduction has led to engine designs with larger fan diameters and higher bypass ratios to increase propulsive efficiency. As a consequence of this trend, the aerodynamic interference with the airframe is increased. Non-axisymmetric exhaust geometries could minimise such interference for coupled configurations. Class Shape Transformation functions are used to define 3D podded engine geometries that are installed on a transonic aircraft configuration. The complete system is assessed at mid-cruise conditions of a representative long-range cruise operation. The assessment is conducted by multi-fidelity computational fluid dynamics computations that are Euler inviscid and Reynolds Averaged Navier Stokes turbulent methods. The correlation between the different fidelities is analysed and a multi-fidelity co-kriging model is developed. The model is applied to predict the behaviour of installed non-axisymmetric exhaust systems and results into a 33% computational benefit compared to single-fidelity surrogates.

1. INTRODUCTION

For civil aviation, the goal of Specific Fuel Consumption (SFC) reduction and propulsive efficiency increase has led to podded underwing engine designs with larger fan diameters and higher bypass ratios. This increases the importance of the propulsion integration aspects for both the engine and airframe. In this coupled problem, the installation effects could affect the installed propulsion system performance with a change in the Net Vehicle Force (NVF) and an alteration of the engine operating point.

Within this context, initial assessments of the installed power plant performance showed good agreement with experimental data using a through-flow nacelle model [1]. Installation effects are demonstrated to be sensitive to the engine size, which becomes significant for larger-diameter engines, and position under the wing. Analyses of different installation positions at cruise conditions demonstrated a net vehicle force (NVF) variation of 1.7% of standard net thrust (F_{NOM}) [2] across the installations considered.

Geometry parametrization enables the definition of geometries for the intakes, nacelles and exhausts using a reduced number of variables. One flexible method for parametrization of aerodynamic shapes is the Class Shape Transformation functions (CST) [3]. It is an analytical approach based on the combination of a class function, which defines the type of geometry, and a shape function, which is decomposed into several polynomials and provides local geometric control. This methodology was extended to the Intuitive approach (iCST) [4] and it has been applied to different propulsion system component shapes as intakes [5,6], nacelles [7] and axisymmetric exhaust systems [8,9]. A first extension of the method to the design of non-axisymmetric exhaust systems for nozzle performance assessment has been conducted [10]. It is based on the combination of longitudinal and azimuthal iCSTs. The modification of circular shapes of the fan cowl through geometric azimuthal variations could ensure sufficient ground and wing clearance and minimize the aerodynamic interference for closely coupled configurations.

The developments in compressible Computational Fluid Dynamics (CFD) methods during the past decades have made it possible to predict with increased fidelity aerodynamic transonic flows in systems such as turbofan exhausts. Recent studies that use Reynolds Averaged Navier Stokes equations (RANS) [11] are focused on single-stream conical nozzles. Research has also been conducted successfully on complex 3D double stream nozzles [12] with satisfactory results compared to experimental data [13].

The problem of the design of exhaust systems for installed power plant configurations relies on the large number of degrees of freedom (DoF) needed. This number is increased for non-axisymmetric configurations. This aspect, combined with the computational time required by CFD simulations, limits the design capabilities. Such Issue could be partially addressed with low order models as surrogates. These models have been proved to predict the afterbody drag coefficient with an uncertainty of +-0.01 for single stream transonic jet flows over large regions of the design space when combined with high-fidelity CFD samples [14]. Other examples of surrogate modelling and application [15,16,17] have been conducted on 2D axisymmetric separate-jet exhausts, where a framework for design and optimization of these geometries is introduced. It has been demonstrated that this approach can rapidly identify dominant design parameters and alleviate adverse flow phenomena that penalise the nozzle performance. A similar implementation has also been applied to intake and nacelle design [18,19,20].

For complete propulsion system-airframe configurations, even the acquisition of enough data to build a surrogate model is unfeasible. In this context, multi-fidelity surrogate models gain interest. These models are trained with a large low-fidelity data set combined with a reduced number of high-fidelity samples. With this approach, the number of high-fidelity points required to predict the function over the design space can be dramatically reduced. Some examples of multi-fidelity surrogates are co-kriging [21], Multi-fidelity Neural Networks [22] and Polynomial Chaos regression [23]. Co-kriging is used in this work due to the reduced data required to build prediction models. As ordinary and universal kriging, co-kriging is a Gaussian regression process initially used in geo-statistics [24]. Previous works have combined different numerical models of different fidelity such as Euler inviscid and RANS methods [25].

The goal of this work is to establish a multi-fidelity framework for the aerodynamic assessment of airframes with installed propulsion systems. This will enable wider explorations of the design space and the reduction of computational resources required. A co-kriging multi-fidelity surrogate model is developed. The model is trained with two sets of data of different fidelity that are Euler inviscid and RANS turbulent methods respectively. The surrogate is applied to predict the aerodynamic performance of non-axisymmetric engine exhaust designs for complete aircraft configurations.

2. METHODOLOGY

2.1. Geometry

The geometry considered within this work is representative of an Ultra High Bypass Ratio Engine (UHBRE) with a bypass ratio of $BPR \approx 18$ and a compact nacelle. The main dimensions of the nacelle are $L_{nac}/R_{hi} = 3.1$ and $R_{nac}/R_{hi} = 0.91$ (Fig. 1a). The engine is mounted under the NASA Common Research Model (CRM) [26] with a pylon and it is pitched ($\theta_{pitch} = 1.75^o$) and toed ($\theta_{toe} = 2.25^o$). 3D geometry parametrizations of the nacelle, intake and exhaust have been developed using iCSTs [3,4,5,6,7,8,9].

A non-axisymmetric parametrization of the fan cowl trailing edge is defined to understand how RANS and Euler simulations correlate for complete aircraft configurations. The parametrization consists of the axial component of a rotation around any desired axis along the azimuthal position of the exhaust. It is represented by two DoF, θ_{shear} or the shear angle

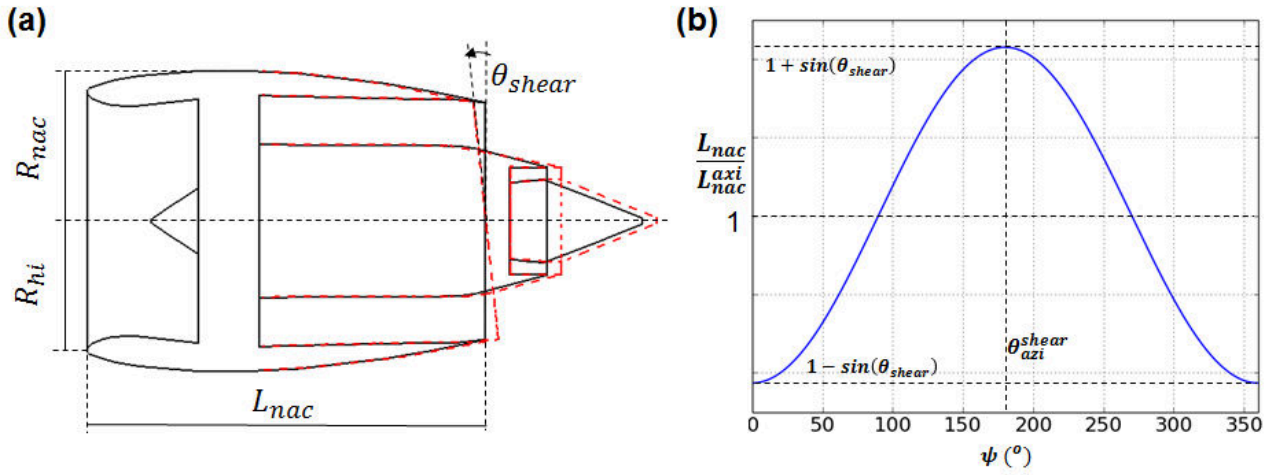

Figure 1. Propulsion system geometry used (a) and shear parametrization applied (b).

and θ_{azi}^{shear} or the azimuthal position with maximum offset due to the transformation (Fig. 1b). The out-board region of the propulsion system corresponds to the azimuthal positions $\psi = 0^o$ to 180^o, while the in-board region ranges from 180^o to 360^o. The design system enables the geometry to be modified from the axisymmetric design to the required sheared case, but also adjusts the radial position to ensure that the bypass and core areas are maintained. The area matching criterion sets a constant core trailing edge radius constraint that results into longer core cowls.

The engine installation location is defined as the position of the upper part of the fan cowl trailing edge with respect to the wing leading edge at a fixed spanwise location (Fig. 2). For non-axisymmetric configurations, the installation position is based on the axisymmetric equivalent design.

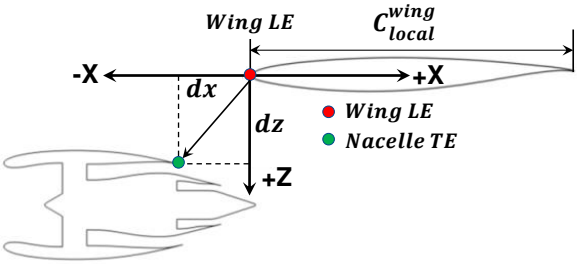

Figure 2. Definition of the installation position.

2.2. Numerical methods

Various CFD methodologies of different fidelities are used. The Euler inviscid approach is selected as the low-fidelity (LF) model and RANS as the high-fidelity (HF) model. The RANS equations are solved with a preconditioned density-based algorithm coupled with the k-ω SST turbulence model. Both CFD models include variations of the air properties with respect to the temperature. Numerical schemes are 2nd order and the default gradient interpolation methods are Green Gauss node based [27].

CFD meshes are fully unstructured and are built following a hybrid approach. It combines tetrahedrons for the potential flow regions of the flow and triangular prisms close to the surfaces to solve the boundary layer. The meshes are of the order of 100M cells for RANS and of 20M cells for Euler simulations (Fig. 3). The hybrid meshing approach for viscous transonic nozzle flows is validated against the experimental measurements undertaken on the static Dual Separate Flow Reference Nozzle (DSFRN) [12,13]. The error obtained with respect to the experiments is of the order of $1e^{-5}$ in terms of exhaust velocity coefficients. The meshing approach for the airframe is validated with the experimental data from the NASA Common Research Model (CRM) [26]. The computational method overpredicts by 14 and 16 drag counts the airframe drag on the clean wing CRM and the throughflow nacelle CRM configurations, respectively [28,29].

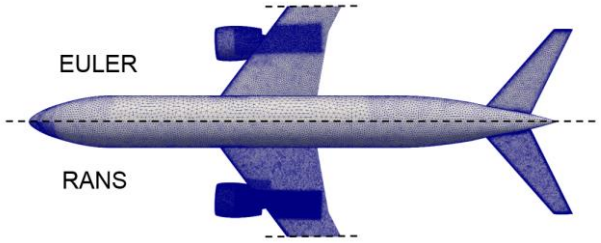

Figure 3. Comparison of Euler and RANS meshes.

All the studies were conducted at mid-cruise operating conditions ($M_\infty = 0.85$, $h = 10688m$) with fixed Fan Nozzle Pressure Ratio ($FNPR = 2.2$) and Core Nozzle Pressure Ratio ($CNPR = 1.57$). The static pressure p_∞, static temperature t_∞, and density ρ_∞ are computed with the International Standard Atmosphere (ISA) model. The internal flow of the engine is only computed at the intake, ducts and nozzles. The fan face is modelled as a mass flow boundary condition where the model is set to capture the intake stream tube. Both bypass and core duct inlets are modelled as fixed total pressure boundary conditions to ensure the desired nozzle pressure ratios. All the walls have been considered non-slip for RANS and slip for Euler computations. The problem is closed with a pressure far field applied to the external boundary and a symmetry condition on the airplane symmetry plane [12].

2.3. Thrust and Drag accounting system

The modified near-field method [30] is used to determine the metrics of interest in an aerodynamic reference frame. The main metric to be maximised for complete aircraft configurations is the net vehicle force (NVF) (Eq. 1). The key aspect is to split this metric into its thrust and drag components (Fig. 4). For simplicity, only the computation of the drag component of the forces is considered, but the formulation on the lift direction follows a similar construct.

$$NVF = (GPF^*)_D^c - D_{nac}^* - F_{G0_D} - D_{A/F} \quad (1)$$

$$= F_{G19_D} + F_{G9_D} - \theta_{CC_D} - \theta_{plug_D} - \theta_{pylon_D} \quad (2)$$

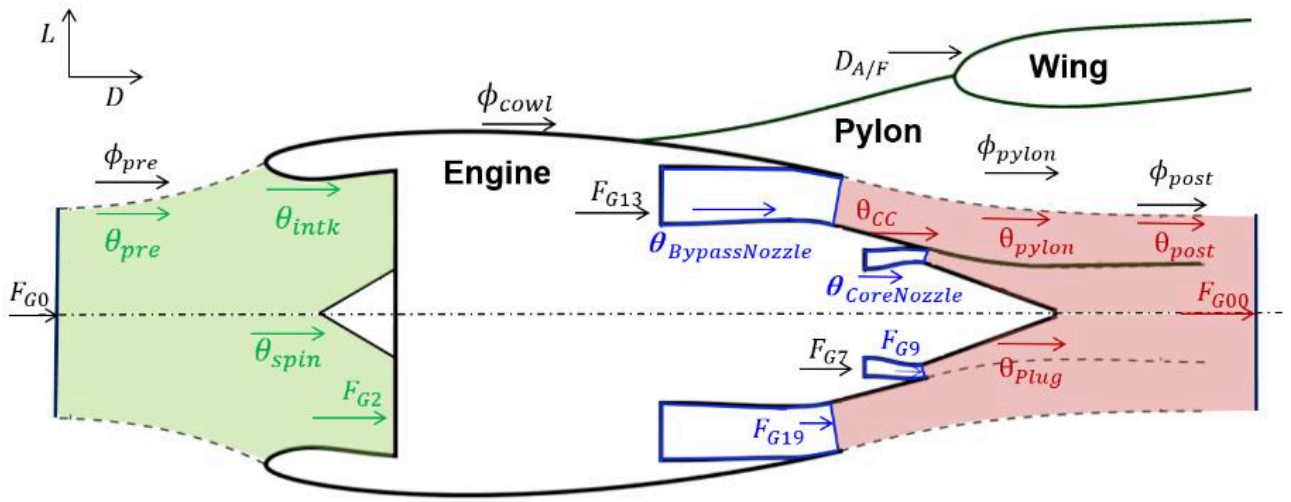

Figure 4. Thrust and drag accounting system schematics.

$$D^*_{nac} = \phi_{pre_D} + \phi_{cowl_D} + \phi_{pylon_D} \quad (3)$$

$$F_{G0} = \dot{m}_{fan} v_\infty \quad (4)$$

GPF^* stands for modified Gross *Propulsive Force* (Eq. 2), D^*_{nac} (Eq. 3) is the modified nacelle drag, $D_{A/F}$ represents the airframe drag and F_{G0} (Eq. 4) is the intake momentum where $\dot{m}_{fan}$ refers to the captured fan mass flow. F_{G9} and F_{G19} stand for gauge forces at nozzle inlets and ϕ and θ refer to drag terms. *IPF* is the *Ideal Propulsive Force* and it is computed with the mass flow obtained with CFD and the velocity of an isentropic and perfectly expanded jet (v^{ideal}) (Eq. 5-6). γ refers to the ratio of specific heats, *R* is the ideal gas constant and T_0 and P_0 stand for total quantities of temperature and pressure respectively.

$$IPF = \dot{m}_{BP_{CFD}} \cdot v^{ideal}_{BP} + \dot{m}_{CR_{CFD}} \cdot v^{ideal}_{CR} \quad (5)$$

$$v^{ideal} = \sqrt{\frac{2\gamma R T_0}{(\gamma - 1)} \left(1 - \left(\frac{p_\infty}{P_0}\right)^{\frac{\gamma-1}{\gamma}}\right)} \quad (6)$$

One of the main nozzle performance indicators is the velocity coefficient (C_v). It is a measure of the deviation of the computed propulsive force with respect to the ideal one. Herein this work the modified version is considered (C^*_V) (Eq. 7).

$$C^*_{v_D} = \frac{(GPF^*)_D}{IPF_{CFD}} \quad (7)$$

Discharge coefficients are also of interest, as they measure the deviation of the computed mass flow with respect to the ideal one $\left(\left(\frac{\dot{m}}{A}\right)_{id}\right)$ at nozzle throats (A^{NOZZ}_{th}) (Eq. 8-9).

$$Cd_{NOZZ} = \frac{\dot{m}_{NOZZ_{CFD}}}{\left(\frac{\dot{m}}{A}\right)_{id} A^{NOZZ}_{th}} \quad (8)$$

$$\left(\frac{\dot{m}}{A}\right)_{id} = P_0 \left(\frac{1}{\min(\lambda, \lambda_{crit})}\right)^{\frac{1}{\gamma}} \cdot \sqrt{\frac{2\gamma}{(\gamma - 1) R T_0} \left(1 - \left(\frac{1}{\min(\lambda, \lambda_{crit})}\right)^{\frac{\gamma-1}{\gamma}}\right)} \quad (9)$$

Drag coefficients are defined to measure the aerodynamics of the nacelle (Eq. 10) and airframe (Eq. 11). The airframe component of the forces includes the wing, tail and fuselage. Drag coefficients take into account the freestream velocity (v_∞) and a reference CRM wing area (A_{ref}) [26]. The equivalent lift coefficients are computed with the lift component of the forces.

$$C^{nac^*}_D = \frac{D^*_{nac}}{\frac{1}{2}\rho v^2_\infty A_{ref}} \quad (10)$$

$$C_D^{A/F} = \frac{D_{A/F}}{\frac{1}{2}\rho v_\infty^2 A_{ref}} \quad (11)$$

To represent typical cruise conditions, the aircraft is trimmed at a constant $C_L^{A/C} = 0.5$. Two angles of attack are solved per case and the solution is linearly interpolated to the target $C_L^{A/C}$. It includes the lift component of the airframe drag, the modified nacelle drag and modified velocity coefficient (Eq. 12).

$$C_L^{A/C} = C_L^{A/F} + C_L^{nac^*} + \frac{(C_v^*)_L \cdot IPF_{cycle}}{\frac{1}{2}\rho v_\infty^2 A_{ref}} \quad (12)$$

2.4. Surrogate modelling using co-kriging

Co-kriging is the surrogate model used for the multi-fidelity assessment [21]. Co-kriging is a Gaussian regression process that uses two sources of data of different fidelity. It consists of two main steps, the training or fitting step and the predictor step.

The predictor step uses the statistical model to predict the behaviour of the high-fidelity function (labelled as 1). The predicted values of $\hat{y}_1$ can be notated in matrixial form (Eq. 13), where only $r(x)$ is related to the points where the function is to be predicted. All the other terms $(\phi_M, \beta, R, y_s, F)$ are matrixes with terms to be fitted along the training step. The correlation matrix (R) is assumed to be dependent on the distance between two data points instead of on their position (x, w) (Eq. 14).

$$\hat{y}_1(x) = \phi_M^T \beta + r^T(x) R^{-1}(y_s - F\beta) \quad (13)$$

$$R_{ij}(\theta_{ij}, x_i, w_j) = \prod_{k=1}^{m} R_k(\theta_{ij}^k, x_{ij}^k - w_{ij}^k), \quad (14)$$

m is the dimensionality of the problem, θ_{ij} is the weight parameter and the sub-indexes i and j are indicative of the levels of fidelity. θ_{ij} are some of the parameters that have to be fitted. The regression models (R_k) employed are Gaussian (Eq. 15) and cubic spline (Eq. 16).

$$R_k(\theta, x^k - w^k)_{GAUSS} = \exp\left(-\theta(x^k - w^k)_j^2\right) \quad (15)$$

$$R_k(\theta, x^k - w^k)_{CSPL} = \begin{cases} 1 - 15\left(\theta|x^k - w^k|\right)^2 + 30\left(\theta|x^k - w^k|\right)^3, & 0 \le x^k - w^k \le 0.2 \\ 1.25\left(1 - \theta|x^k - w^k|\right)^3, & 0.2 < x^k - w^k < 1 \\ 0, & x^k - w^k \ge 1 \end{cases} \quad (16)$$

The model is fitted through the maximization of the likelihood function. The implementation reduces the number of independent parameters by the derivation of analytical expressions for the optimum values of some of them (Eqs. 17-18).

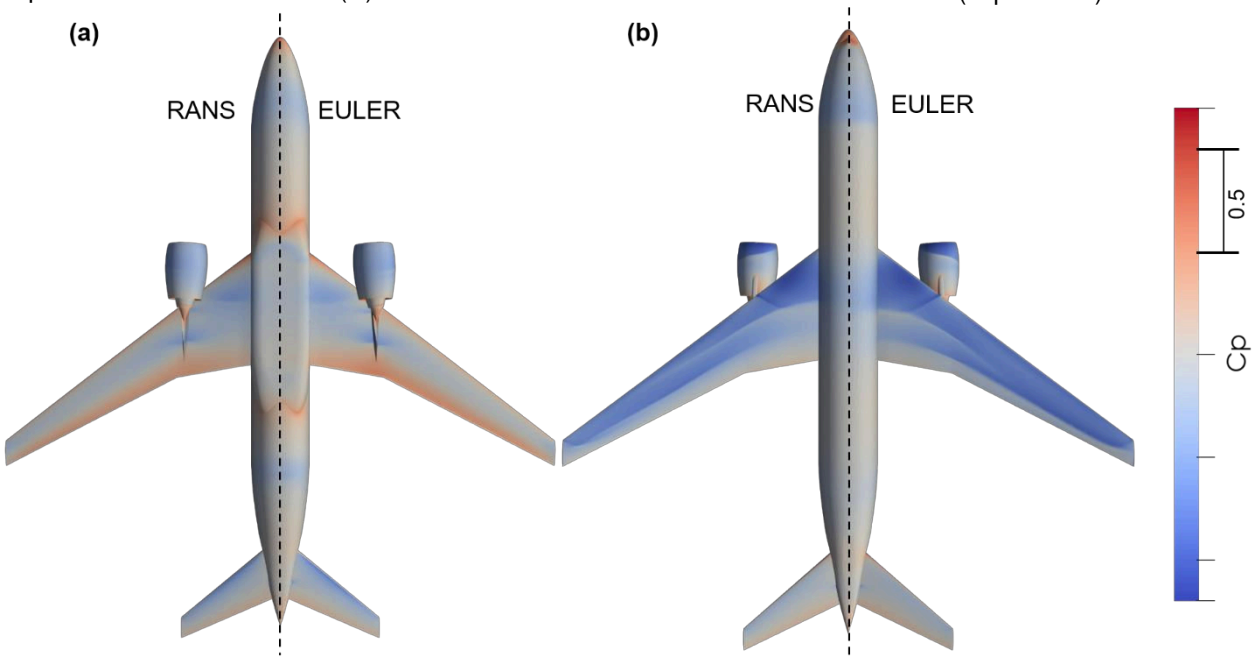

Figure 5. Pressure distribution for the full airframe-engine system resolved with Euler and RANS models at the underside (a) and topside (b) views at an angle of attack of 2º

$$ln[L(\theta_{11}, \theta_{22}, \theta_{12})] = -\frac{1}{2}[(n_1 + n_2) \cdot \ln(\sigma_1^2) + \ln(|R|)] \quad (17)$$

$$\theta_{11}, \theta_{22}, \theta_{12} = argmax[\ln(L)] \quad (18)$$

n_1 and n_2 correspond to the number of high and low-fidelity data samples respectively and σ_1^2 refers to the correlation between LF and HF data. The maximisation of this function is conducted with the *COBYLA* optimization algorithm [31].

3. RESULTS AND DISCUSSION

3.1. Euler and RANS CFD assessment

Euler model simulations are used together with a reduced number of RANS simulations in the multi-fidelity framework presented. Euler simulations are 36 times faster with respect to RANS (Table 1.) This opens the opportunity to cover wider design spaces using Euler computations and assess fewer points with RANS.

Table 1. Comparison of Euler and RANS computational performance.

Type	***Cores***	***Mesh***	***Time per case***
RANS	128	100M cells	36t
Euler	128	20M cells	t

The first stage towards the establishment of the multi-fidelity approach is to understand the difference between RANS and Euler simulations. A back to back comparison is conducted in terms of the flow field of an installed propulsion system with an axisymmetric exhaust. A Design Space Exploration (DSE) of the shear parametrization applied to the same engine is evaluated in terms of the performance metrics. The DSE is conducted using both Euler and RANS models.

The complete airframe-engine system is assessed with the engine installed at position $dx/C = 0$ and $dz/C = 0.075$ (Figs. 5-6). The configuration with an axisymmetric exhaust system (Figs 5, 6a and 6b) is used as a reference to assess the benefits produced by the non-axisymmetric exhausts. The flow field is analysed in terms of pressure coefficient distributions (Eq. 19).

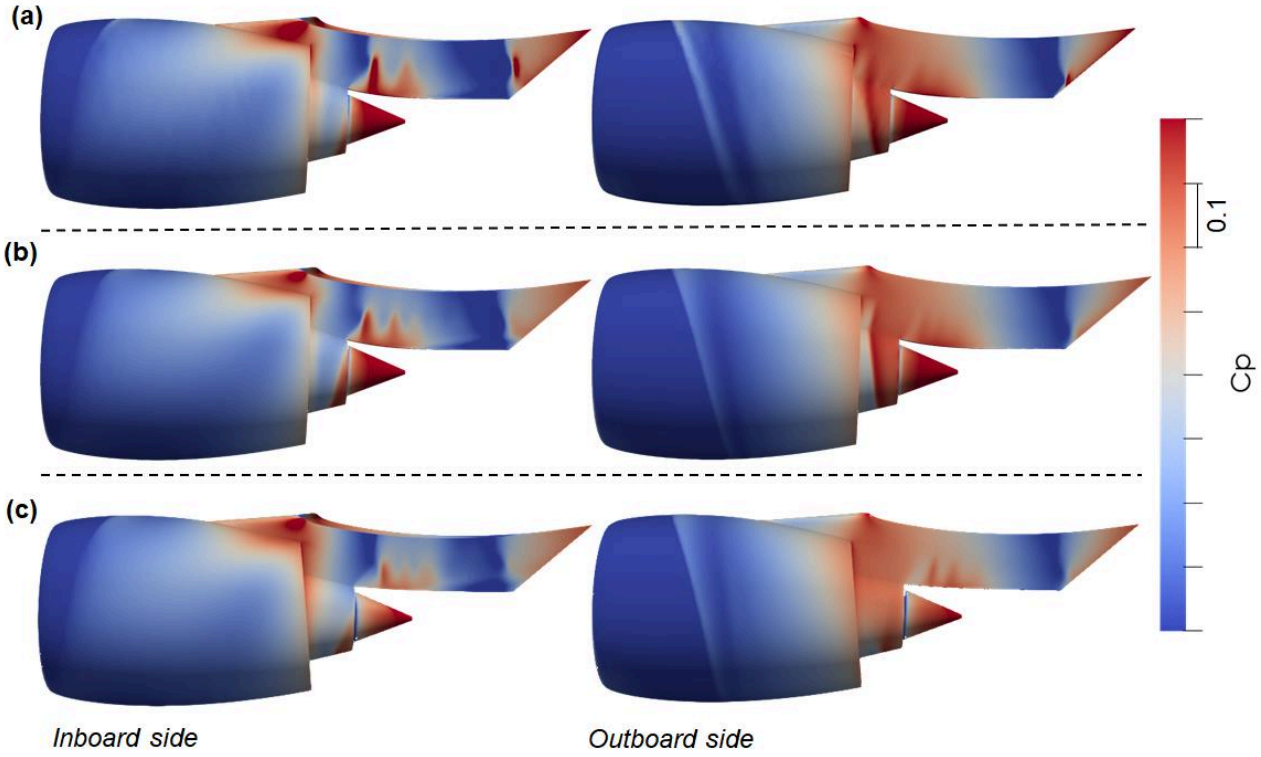

Figure 6. Pressure distribution on the in-board and out-board sides of the engine. It includes the axisymmetric engine resolved with the Euler (a) and RANS (b) models as well as the design with $\theta_{shear} = 6^o$ and $\theta_{azi}^{shear} = 180^o$ evaluated with RANS (c).

$$Cp = (p - p_\infty)/\left(\frac{1}{2}\rho_\infty v_\infty^2\right) \quad (19)$$

Overall the flow is well predicted by the Euler model, but some differences can be observed. In the airframe underside view (Fig. 5a) the lower-fidelity model overpredicts the strength of the shock waves located on the channel flow composed by the fuselage, pylon and engine. This effect is related to the lack of viscous dissipation. In addition, all the shock waves predicted by the Euler computations are slightly displaced downstream. The pressure distributions on the engine (Figs. 6a-6b) illustrate that the Euler solution accurately represents the

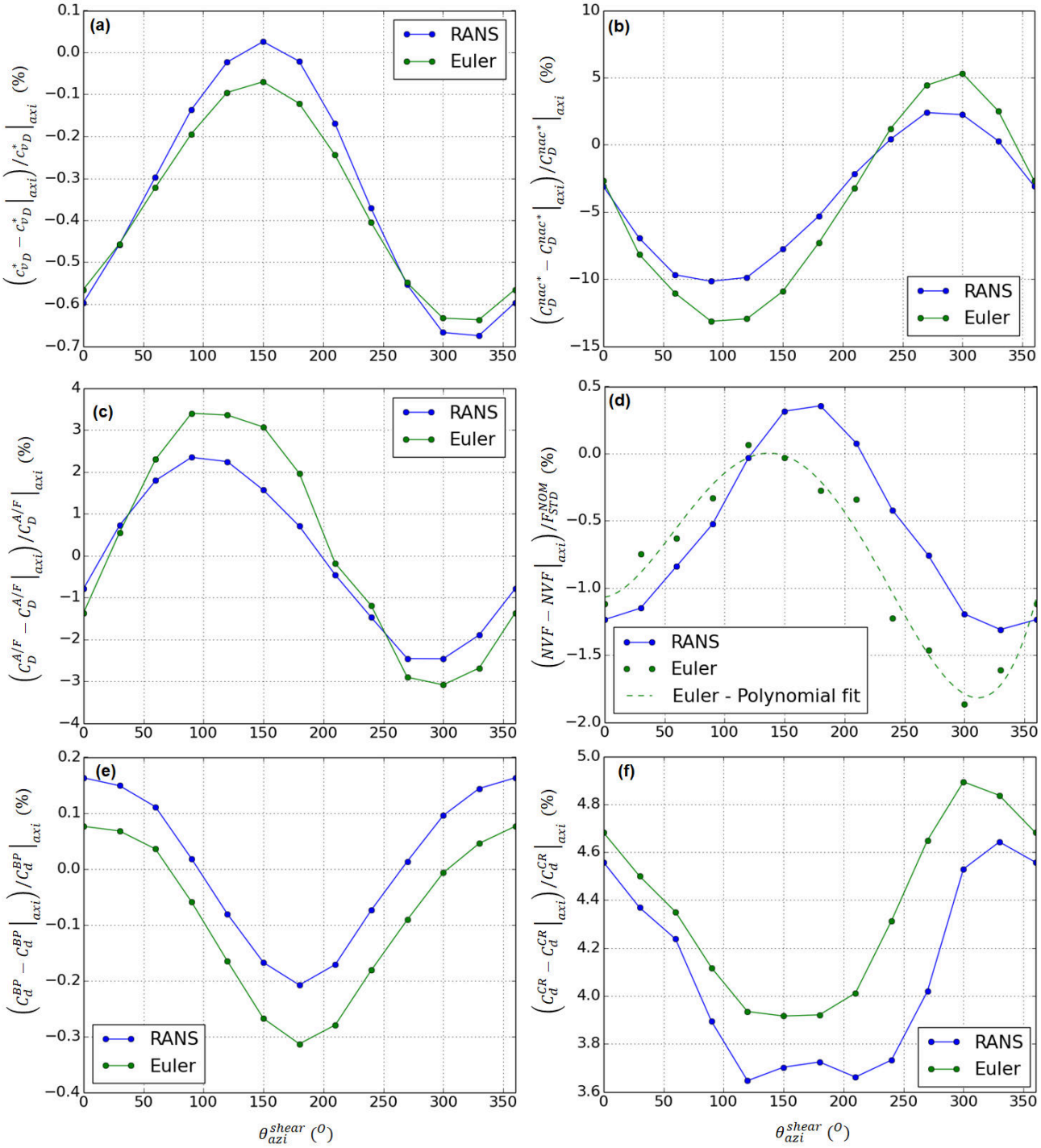

Figure 7. Results summary of the shear parametrization DSE. Results of $C^*_{v_D}$ (a), C_D^{nac*} (b), $C_D^{A/F}$ (c), NVF (d), C_d^{BP} (e) and C_d^{CR} (f) are displayed for both Euler and RANS computations.

topology of the under-expanded jet flow ejected from the bypass nozzle. There are minor differences in the flow at the in-board side of the nacelle. Additionally, the strength of the discontinuities is greater in Euler for the first and pylon trailing edge shock waves. The pressurisation of the core cowl seems to be reduced compared to the RANS equivalent. In opposition, it is increased on the plug. On the out-board side, the strength of pylon trailing edge shock and the expansion after the nacelle shock wave are both magnified if the Euler model is used.

A design space exploration (DSE) of the shear parametrization is conducted with a fixed shear angle $\theta_{shear} = 6^o$. θ_{azi}^{shear} varies around the azimuthal position of the fan cowl trailing edge ($\theta_{azi}^{shear} = 0^o \; to \; 360^o$). The RANS model predicts a maximum of $C_{v_D}^*$ (Fig. 7a) around $\theta_{azi}^{shear} = 150^o$. The reason is the modification of the thrust vector and its closer alignment with the drag direction, which implies a reduction of the thrust loss due to pitch and toe angles. The difference of the exit plane inclination of both nozzles slightly modifies the exhaust direction of the bypass flow with respect to the core.

The $C_{D_{nac}}^*$ (Fig. 7b) is greatly reduced at $\theta_{azi}^{shear} = 0^o \; to \; 200^o$ because the fan cowl is shortened on the regions with higher suction of the in-board side. On the other hand, $C_{D_{A/F}}$ (Fig. 7c) is increased along the same azimuthal span. The changes to the airframe drag are produced by a mixture of effects. First, there is an increase of induced drag due to the trim procedure. The exhaust force contributes less to the system lift because of the changes in thrust vector. $C_{L_{A/F}}$ is consequentially increased and it penalises $C_{D_{A/F}}$. The fact that there is a difference of $\Delta\theta_{azi}^{shear} = 60^o$ between the predicted peaks of $C_{D_{A/F}}$ and $C_{v_D}^*$ suggests that other effects that increase the parasitic drag are also present.

In general, Euler computations follow the same behaviour and trends of RANS (Fig. 7). The distribution and gradients of $C_{v_D}^* = f(\theta_{azi}^{shear})$ are well represented by the Euler model. Main sinusoidal characteristics are captured where the peak-to-peak variation is around 0.15% less than the RANS equivalent. The low-fidelity model does not predict any benefit compared to its axisymmetric reference. In contrast, the RANS model predicts a maximum benefit of $\Delta C_{v_D}^* = 0.025\%$. The amplitude of $C_{D_{nac}}^* = f(\theta_{azi}^{shear})$ is over predicted by $\Delta C_{D_{nac}}^* = 5\%$ in Euler computations. In addition, the local maximum of $C_{D_{nac}}^*$ evaluated in the Euler framework is at 300^o relative to the 270^o obtained with RANS. The Euler simulations overpredict the local maximum and minimum values of $C_{D_{A/F}}$ by 1.6% compared with the RANS results. The gradient is not as effectively captured as for the other metrics because some statistical noise is induced.

$C_{d_{BP}}$ is decreased with respect to the axisymmetric cases at $\theta_{azi}^{shear} = 100^o \; to \; 270^o$ (Fig. 7e). The reason is that the bypass jet is slightly deflected towards the pressure side of the wing for this range of azimuthal positions. The static pressure on the pressure side of the wing is then increased and the in-board side shock wave over the core cowl is mitigated (Fig. 6c). Both effects increase the static pressure perceived by the bypass nozzle and increase the bypass flow suppression. Euler computations follow the same trends but are offset by $\Delta C_{d_{BP}}|_{Euler} - \Delta C_{d_{BP}}|_{RANS} = -0.1$. A similar effect is observed for $C_{d_{CR}}$ (Fig. 7f). The RANS results of $C_{d_{CR}}$ predict two local minima at $\theta_{azi}^{shear} = 120^o$ and $\theta_{azi}^{shear} = 210^o$. This is a 3D effect produced by the wake of the pylon and it is reduced at $\theta_{azi}^{shear} = 180^o$ because the bypass jet deflection is normal to the pylon heatshield. This flow feature is not predicted by the Euler model, which may indicate that it comes from a viscous related source. Again, the lower-fidelity model follows the same trends as the high-fidelity one. It has a magnitude offset of $\Delta C_{d_{CR}} = 0.2$ measured at the peaks and a difference in azimuthal position of $\Delta\theta_{azi}^{shear} = 30^o$. All the configurations predict benefits on the core discharge coefficient up to 5% compared to the axisymmetric reference case.

If all the force terms are added, the overall net vehicle force (NVF) is obtained (Fig. 7d). The RANS solution suggests that the NVF follows a Gaussian distribution with predicted benefits up to 0.4% at $\theta_{azi}^{shear} = 120^o \; to \; 220^o$. The optimum design assessed ($\theta_{azi}^{shear} = 180^o$) (Fig. 6c) reduces the strength of the shock wave located on the core cowl. This penalises the bypass flow discharge by a 0.3% through an increased pressurisation of the core cowl. It also benefits the core jet expansion and discharge. The increase in core cowl length as a consequence of the shear parametrization results into strength reduction and downstream displacement of the jet shock waves, which confirms the core flow discharge coefficient behaviour. NVF shows the biggest differences between RANS and Euler computations. The discrepancies in terms of amplitude and phase previously stated propagate to the NVF as well as the scatter observed on the airframe drag for the LF model. The result is a noisy LF data set that is

displaced azimuthally ($\theta_{\text{azi}}^{shear}|_{Euler} - \theta_{\text{azi}}^{shear}|_{RANS} \approx -30^o$) and in magnitude ($\Delta NVF|_{Euler} - \Delta NVF|_{RANS} \approx 0.2\%$).

Overall the RANS simulations show a potential improvement of around 0.4% of the standard nominal net thrust for the best non-axisymmetric configuration tested. The maximum benefit of NVF is under predicted by the Euler model by 0.3%. The solutions of the same metric have statistical noise if the low-fidelity model is used. The scatter mostly propagates from $C_{D_{A/F}}$. Despite the differences, Euler is clearly accurate enough to construct a low fidelity data set for wider design space explorations and multi-fidelity surrogate modelling.

3.2. Surrogate model application

The implementation of the co-kriging method is verified using an analytical case representative of two functions with different levels of fidelity. These two functions (Eqs. 20-21) have been used in the literature to verify multi-fidelity models [21,25]. y_1 and y_2 stand for high and low fidelity function respectively.

$$y_1 = (6x-2)^2 \sin(12x-4), \qquad x \in [0,1] \qquad (20)$$

$$y_2 = 0.5y_1 + 10(x-0.5) - 5, \qquad x \in [0,1] \qquad (21)$$

The co-kriging models obtained using Gaussian and cubic spline correlation functions are presented together with single-fidelity kriging models trained with y1 and y2 respectively (Fig. 8). 4 HF samples are combined with 11 LF points. The results highlight how a surrogate model can be improved by adding lower-fidelity data, as the kriging model through y1 is visibly inaccurate. Co-kriging results demonstrate the improved performance of the cubic spline function with respect to the Gaussian correlation for this case. The Gaussian model does not accurately represent the whole high-fidelity function, but the local minimum region is reasonably well predicted. The prediction of the cubic-spline function is in good agreement with the literature [21,25].

The prediction models are applied to the Euler and RANS results to determine the effect of θ_{azi}^{shear} on the overall aircraft NVF (Fig. 7d). The goal is to identify the potential benefit in terms of reduction of the number of RANS simulations required with respect to a single-fidelity kriging model. A statistical sampling convergence analysis is performed by a successive increase of the number of high-fidelity samples used in the training step (Fig. 9). At each iteration, all the combinations of *r* HF samples are

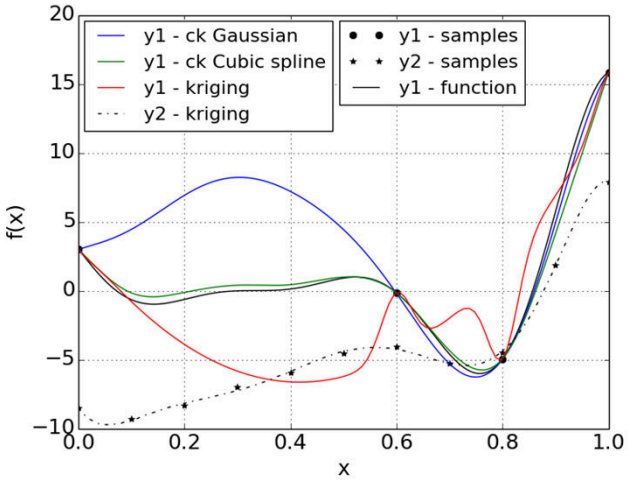

Figure 8. Co-kriging model verification test case.

used from the total data set *n* (Eq. 22). The number of LF samples used in the multi-fidelity models is set to 13. The analysis is applied to the prediction of the NVF in terms of the maximum evaluated value (ΔNVF_{max}) (Fig. 9a), its azimuthal position ($\theta_{\text{azi}}^{shear}|_{\Delta NVF_{max}}$) (Fig. 9b) and the root mean square deviation ($RMSD$) with respect to all the HF samples (Eq.23) (Fig. 9c).

$$nHF(r) = \frac{n!}{r!\,(n-r)!} \qquad (22)$$

$$RMSD = \sqrt{\frac{\sum_{i=1}^{n}(\hat{y}_i - y_i^{HF})}{n}} \qquad (23)$$

The Gaussian co-kriging model achieves monotonic convergency with 5 HF samples in ΔNVF_{max} as a function of $\theta_{\text{azi}}^{shear}$ (Fig. 9a). The same model shows a discontinuity in convergence at $11 \leq \text{nHF} \leq 13$. Such discontinuity is consequence of oversampling, as too many high-fidelity samples are used. The model is then unable to properly fit the curve. Consequentially, the ratio of samples of different fidelity should be $nHF/nLF < 0.8$. In opposition to the Gaussian co-kriging surrogate, the kriging model converges non-monotonically for ΔNVF_{max}. It is considered that the peak magnitude is converged if 8 or more HF samples are used, as the trend remains constant. The prediction of ΔNVF_{max} is worse for the multi fidelity surrogate that uses the cubic spline model. It does not converge because of its increased sensitivity to the statistical noise that comes from the LF function. Both Gaussian multi-fidelity and single-fidelity models converge on $\theta_{\text{azi}}^{shear}|_{\Delta NVF_{max}}$ with 6 HF samples within +-15^o (Fig. 9b). The cubic spline-based model needs 8 to reach

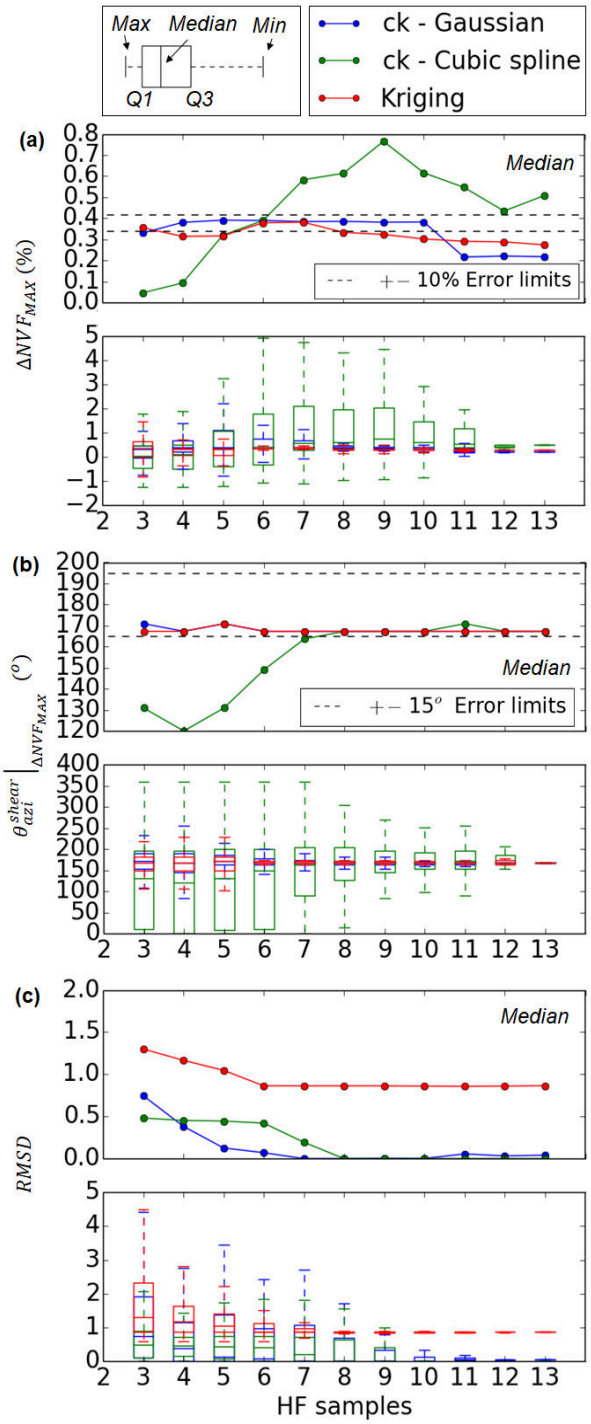

Figure 9. Sampling convergence analysis for the prediction of ΔNVF_{MAX} (a), $\theta_{azi}^{shear}|_{\Delta NVF_{MAX}}$ (b) and $RSMD$ (c).

the same level of accuracy. The RMSD (Fig. 9c) indicates that all the data points of the HF function are better approximated by both co-kriging models than for the single-fidelity surrogate.

The data of the cubic spline co-kriging surrogate

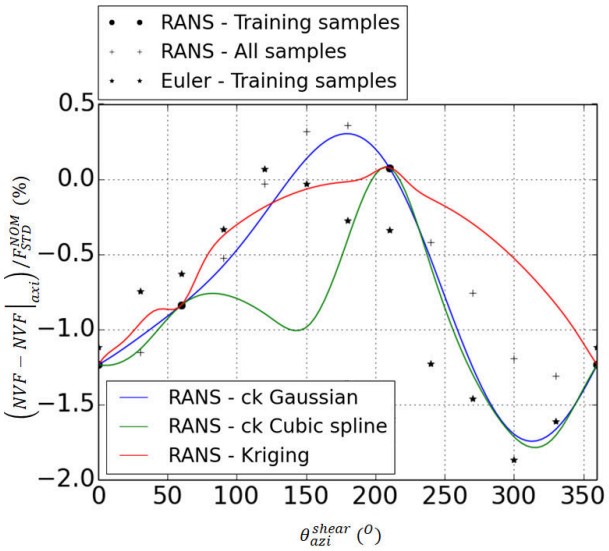

Figure 10. Prediction models of the NVF using 4 RANS samples.

prediction is more disperse compared to the other models tested. This highlights again the adverse influence of the statistical noise for this model. The Gaussian model solution has some dispersion for $nHF < 6$. This effect manifests the importance of the sampling strategy for a reduced number of training samples. An improper distribution of samples could result into wrong predictions and additional cost within an optimisation system.

The improved performance of the Gaussian co-kriging model with respect to the other two is confirmed if one random case with 4 HF samples is considered (Fig. 10). It is the only model that resembles the shape, gradients and peak value of $\Delta NVF = f(\theta_{azi}^{shear})$. In addition, the statistical noise is filtered out of the prediction. The poor behaviour of the cubic spline model in the presence of scattered data is also highlighted. At $\theta_{\mathrm{azi}}^{shear} = 0^o - 100^o$ the cubic spline-based model follows the trends of the lower-fidelity data and results into a shape that diverges from the RANS predicted curve. The kriging model is not able to reproduce the main trends of the high-fidelity function, nor the peak location and value for this case.

The use of co-kriging for multi-fidelity analysis of non-axisymmetric exhaust systems has been proved to be potentially useful. The peak value of the NVF can be converged within the acceptable bounds with 23% less HF samples and increased accuracy than for single-fidelity kriging. In terms of computational time, it would result into a benefit of around 33% if Euler and RANS are considered (Table 1) compared to RANS only.

4. CONCLUSIONS

The work establishes a first step towards the multi-fidelity assessment of installed configurations with non-axisymmetric exhaust systems.

- The non-axisymmetric shear parametrization of the nacelle trailing edge can benefit the performance of the combined power plant-airframe system. The optimum shear azimuthal position assessed is $\theta_{azi}^{shear} = 180^o$ with a benefit of $\Delta NVF = 0.4\%$ of standard nominal net thrust with respect to the axisymmetric reference.

- The improved performance of a multi-fidelity co-kriging model against the single fidelity kriging is proved for non-axisymmetric exhaust behaviour prediction of. The co-kriging model provides a good representation of the high-fidelity function and it exhibits potential computational time benefits of 33% with respect to single-fidelity kriging if Euler and RANS models are considered.

5. ACKNOWLEDGMENTS

This work was partially funded by Rolls-Royce plc.

6. REFERENCES

1. Stankowski, T., MacManus, D. G., Sheaf, C. & Christie, R. (2016). Aerodynamics of aero-engine installation. *J. Aerospace Engineering*. **230**(14) 2673-2692.

2. Stankowski, T. P., MacManus, D. G., Robinson, M. & Sheaf, C. T. (2017). Aerodynamic Effects of Propulsion Integration for High Bypass Ratio Engines. *Journal of Aircraft*, **54**(6), 2270-2284.

3. Kulfan, B., M. & Bussoletti, J., E. (2006). Fundamental Parametric Geometry Representations for Aircraft Component Shapes, 11th AIAA/ISSMO Multidisciplinary Analysis and Optimization Conference, Virginia, USA.

4. Zhu, Z. & Qin, N. (2014). Intuitive Class/Shape Function Parameterization for Airfoils. *AIAA Journal*. **52** (1), 17–24.

5. Christie, R., Heidebrecht, A., & MacManus, D. (2016). An Automated Approach to Nacelle Parameterization Using Intuitive Class Shape Transformation Curves. *Journal of Engineering for Gas Turbines and Power*. **139**(6), 062601-1-9.

6. Christie, R., Robinson, M., Tejero, F. & MacManus, D. G. (2019). The use of hybrid intuitive class shape transformation curves in aerodynamic design. *Aerospace Science and Technology*. **95**, 105473-1-13.

7. Heidebrecht, A., Stankowski, T., & MacManus, D. (2016) Parametric Geometry and CFD Process for Turbofan Nacelles. *Proceedings of ASME, Turbomachinery Technical Conference and Exposition*, South Korea.

8. Goulos, I., Stankowski, T., Otter, J., MacManus, D., Grech, N., & Sheaf, C. (2016) Aerodynamic Design of Separate-Jet Exhausts for Future Civil Aero-engines Part I: Parametric Geometry Definition and Computational Fluid Dynamics Approach. *J. Eng. Gas Turbines and Power*. **138**(8), 081201-1-14.

9. Goulos, I., Stankowski, T., MacManus, D., Woodrow, P., & Sheaf, C. (2018) Civil Turbofan Engine Exhaust Aerodynamic: Impact of bypass nozzle after-body design. *Aerospace Science and Technology*. **73**.

10. Otter, J., J. (2015-2018). Aerodynamics and Performance of Civil Aero-Engine Exhaust Systems. *Cranfield University, PhD Thesis.*

11. Zhang, Y., Chen, H., Zhang, M., Zhang, M., LI, Z. & Fu, S. (2015). Performance prediction of conical nozzle using Navier–Stokes computation. *AIAA J. of Propulsion and Power*, **31**(1), 192–203.

12. Otter, J. J., Goulos, I., MacManus D. G. & Slaby, M. (2018) Aerodynamic Analysis of Civil Aeroengine Exhaust Systems Using Computational Fluid Dynamics. *AIAA J. of Propulsion and Power*. **34**(5), 1552-1165.

13. Mikkelsen, K. L., Myren, D. J., Dahl, D.G. & Christiansen, M. D. (2015) Initial subscale performance measurements of the AIAA dual separate flow reference (DSFR) nozzle. *AIAA Propulsion and Energy Forum, 51st AIAA Joint Propulsion Conference*, Florida, USA.

14. Zuccolo, G., Christie, R., MacManus, D., Goulos, I., Martin, P. (2020). Low Order Model for Transonic Afterbody Aerodynamic Characteristics. *Proceedings of AIAA SciTech Forum*.

15. Goulos, I., Otter, J., Stankowski,T, MacManus, D., Grech, N. & Sheaf, C. (2018). Design optimisation of separate-jet exhausts for the next generation of civil aero-engines. *The*

Aeronautical Journal. **122**(1256), 1586-1605

16. Goulos, I., Otter, J., Stankowski, T., MacManus, D., Grech, N., & Sheaf, C. (2016). Aerodynamic Design of Separate-Jet Exhausts for Future Civil Aero-engines Part II: Design Space Exploration, Surrogate Modelling, and Optimization. *J. Eng. Gas Turbines and Power*. **138**(8), 081202-1-12.

17. Giangaspero, G., MacManus, D. G. & Goulos, I. (2019). Surrogate models for the prediction of the aerodynamic performance of exhaust systems. *Aerospace Science and Technology.* **92**, 77-90.

18. Heidebrecht, A. & MacManus, D. G. (2019). Surrogate model of complex non-linear data for preliminary nacelle design. *Aerospace Science and Technology*. **84**, 399-411.

19. Tejero, F., Robinson, M., MacManus, D. G. & Sheaf, C. (2019). Multi-objective optimisation of short nacelles for high bypass ratio engines. *Aerospace Science and Technology*. **91**, 410-421.

20. Tejero, F., MacManus, D. G. & Sheaf, C. (2019). Surrogate-based aerodynamic optimisation of compact nacelle aero-engines. Aerospace Science and Technology. **93**, 105207.

21. Han Z., Gortz, S. & Gortz, Z. (2012). Alternative Cokriging Model for Variable-Fidelity Surrogate Modeling. AIAA Journal Technical Notes. 50(5), 1205-1210.

22. Shah. H., Hosder, S., Koziel, S., Tesfahumegn, Y. A. & Leifsson, L. (2015). Multi-fidelity robust aerodynamic design optimization under mixed uncertainty. *Aerospace Science and Technology*. 45, 17-29.

23. Meng, X. & Karniadakis, G. E. (2019) A composite neural network that learns from multi-fidelity data: Application to function approximation and inverse PDE problems. *J. of Computational Physics*.

24. Bancheri, M., Seafin, F., Bottazzi, M., Abera, W., Formetta, G. & Rigon R. (2018). The design, deployment, and testing of kriging models in GEOframe with SIK-0.9.8. Geosci. Model Dev. **11**, 2189–2207.

25. Kaya, H., Tiftikç, H., Kutluay, U., & Sakarya, E. (2019). Generation of surrogate-based aerodynamic model of an UCAV configuration using adaptive co-kriging method. *Aerospace Science and Technology*.

26. Rivers, M. B. & Dittberner, A. (2011). Experimental Investigations of the NASA Common Research Model in the NASA Langley National Transonic Facility and NASA Ames 11-Ft Transonic Wind Tunnel (Invited).*49th AIAA Aerospace Sciences Meeting including the New Horizons Forum and Aerospace Exposition*. AIAA Paper 2011-1126.

27. Ansys Inc, 275 Technology drive, Canonsburg, PA 15317. ANSYS FLUENT User's Guide.

28. Tejero, F., Goulos, I. & MacManus, D. G. (2020). Effects of Aircraft Integration on Compact Nacelle Aerodynamics. *The AIAA SciTech Forum*.

29. Levy, D. W. et al. (2014). Summary of Data from the Fifth Computational Fluid Dynamics Drag Prediction Workshop. *Journal of Aircraft*. **51**(4), 1194-1213

30. AGARD. (1981). Aerodynamics of Power Plant Installation. Advisory Group for Aerospace Research and Development*, AGARD-CP-301*.

31. Varoquaux, G., Gouillart, E., Vahtras, O. and de Buyl, P. (2019). Scipy Lecture Notes.

2020-02-28

Multi-fidelity assessment of exhaust systems for complete engine-airframe integrations

Hueso Rebassa, Josep

Unknown